Physics in Medicine & Biology

IPEM Institute of Physics and Engineering in Medicine

NOTE • OPEN ACCESS

Stopping power and range estimations in proton therapy based on prompt gamma timing: motion models and automated parameter optimization

To cite this article: Julius Werner *et al* 2024 *Phys. Med. Biol.* **69** 14NT02

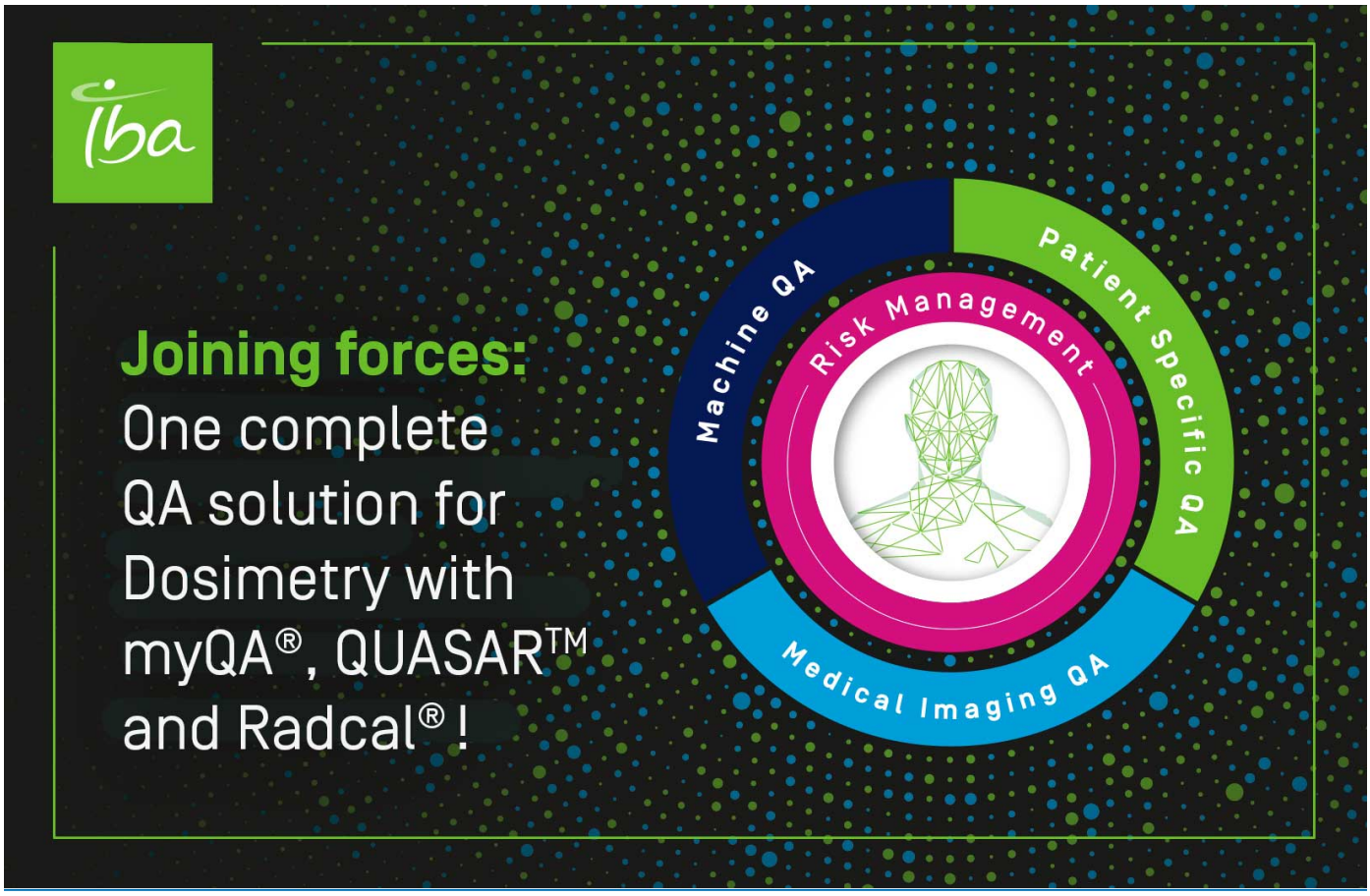

IOP Publishing Phys. Med. Biol. 69 (2024) 14NT02 https://doi.org/10.1088/1361-6560/ad5d4b

Physics in Medicine & Biology

IPEM Institute of Physics and Engineering in Medicine

NOTE

Stopping power and range estimations in proton therapy based on prompt gamma timing: motion models and automated parameter optimization

Julius Werner[1,*], **Francesco Pennazio**[2], **Niklas Schmid**[3], **Elisa Fiorina**[2], **Davide Bersani**[4], **Piergiorgio Cerello**[2], **Jona Kasprzak**[1], **Nicola Mosco**[2], **Sahar Ranjbar**[2,5], **Roberto Sacchi**[2,5], **Veronica Ferrero**[2,6] and **Magdalena Rafecas**[1,6]

[1] Institute of Medical Engineering, Universität zu Lübeck, Lübeck, Germany
[2] Istituto Nazionale di Fisica Nucleare, Sezione di Torino, Torino, Italy
[3] Automatic Control Laboratory, ETH Zürich, Zürich, Switzerland
[4] Istituto Nazionale di Fisica Nucleare, Sezione di Pisa, Pisa, Italy
[5] Dipartimento di Fisica, Università degli Studi di Torino, Torino, Italy
[6] These authors share last authorship.
[*] Author to whom any correspondence should be addressed.

E-mail: friedemann.werner@uni-luebeck.de

Keywords: proton therapy, treatment verification, prompt gamma timing, stopping power, range monitoring, Monte-Carlo simulations, optimization

RECEIVED
23 December 2023

REVISED
11 June 2024

ACCEPTED FOR PUBLICATION
28 June 2024

PUBLISHED
15 July 2024

Abstract

Objective. Particle therapy treatments are currently limited by uncertainties of the delivered dose. Verification techniques like Prompt-Gamma-Timing-based Stopping Power Estimation (PGT-SPE) may allow for reduction of safety margins in treatment planning. *Approach.* From Prompt-Gamma-Timing measurements, we reconstruct the spatiotemporal distribution of prompt gamma emissions, which is linked to the average motion of the primary particles. The stopping power is determined by fitting a model of the average particle motion. Here, we compare a previously published implementation of the particle motion model with an alternative formulation and present two formulations to automatically select the hyperparameters of our procedure. The performance was assessed using Monte-Carlo simulations of proton beams (60 MeV–219 MeV) impinging on a homogeneous PMMA phantom. *Main results.* The range was successfully determined within a standard deviation of 3 mm for proton beam energies from 70 MeV to 219 MeV. Stopping power estimates showed errors below 5% for beam energies above 160 MeV. At lower energies, the estimation performance degraded to unsatisfactory levels due to the short range of the protons. The new motion model improved the estimation performance by up to 5% for beam energies from 100 MeV to 150 MeV with mean errors ranging from 6% to 18%. The automated hyperparameter optimization matched the average error of previously reported manual selections, while significantly reducing the outliers. *Significance.* The data-driven hyperparameter optimization allowed for a reproducible and fast evaluation of our method. The updated motion model and evaluation at new beam energies bring us closer to applying PGT-SPE in more complex scenarios. Direct comparison of stopping power estimates between treatment planning and measurements during irradiation would offer a more direct verification than other secondary-particle-based techniques.

1. Introduction

Prompt Gamma Timing (PGT) is a promising concept that exploits the time of flight (TOF) of both the primary protons and the resulting prompt gamma (PG) radiation to infer possible range deviations in proton therapy. The TOF spectra hold indirect information about the spatial and temporal distribution of PG emissions, which in turn are correlated with the motion and range of the primary particles. This

information can be used to ensure compliance of the delivered treatment with the treatment plan. Since the introduction of PGT as a fast and cheap treatment monitoring concept a decade ago (Golnik *et al* 2014), different detection and evaluation approaches have been proposed (Werner *et al* 2019, Jacquet *et al* 2021, Schellhammer *et al* 2022).

We previously introduced Spatiotemporal Emission Reconstruction from Prompt Gamma Timing (SER-PGT), a method for estimating the combined spatial and temporal distribution of the emitted PG using PGT spectra from several detectors (Pennazio *et al* 2022), together with an optimization procedure to solve the underlying inverse problem. In addition to providing an estimate of the beam range, we hypothesize that the postprocessed spatiotemporal distribution allows the stopping power to be inferred (Ferrero *et al* 2022b). In the latter publication we have shown, as a proof of principle, that this is possible by fitting the Bortfeld motion model to the postprocessed spatiotemporal distribution.

Our long-term goal is to be able to provide estimates for quality assurance of other stopping power calculations done for treatment planning (e.g. from x-ray Computed Tomography or proton Computed Tomography). The PG radiation measurements would take place during the beam delivery, hence the comparison of stopping power measurements allows direct verification of the tissue properties and anatomy assumed in the treatment plan. To our knowledge, our approach, termed Prompt-Gamma-Timing-based Stopping Power Estimation (PGT-SPE), is currently the only one available in literature aiming to directly estimate the stopping power during the treatment. Nevertheless, our investigation is at an exploratory stage and, as such, requires further improvements to overcome current limitations. So far, PGT-SPE has only been demonstrated with Monte-Carlo simulations of homogeneous targets and a limited number of initial proton beam energies (Ferrero *et al* 2022b). A preliminary investigation with a reduced set of PGT detectors was published in Ferrero *et al* (2022a). This work aims to address some open challenges in PGT-SPE in preparation to extend our investigations to inhomogeneous targets.

A bottleneck of our current implementation lies in the time-consuming and tedious configuration of the analysis of the spatiotemporal distribution. For each beam energy, an appropriate number of iterations and a threshold needs to be determined. Doing this manually is feasible for a few cases, but becomes cumbersome for large evaluations, especially since the tuning needs to be repeated each time the beam parameters, target, or estimation procedure change. To automate the tuning, we propose a data-driven optimization of the algorithm's hyperparameters. Using this automation, we were able to expand the number of evaluated beam energies to 17 ranging from 63 MeV to 219 MeV, compared to six beam energies ranging from 110 MeV to 219 MeV in Ferrero *et al* (2022b). Another issue is how to handle the data from the spatiotemporal distribution for model fitting. Here, we present an alternative implementation of the motion model to address some limitations of the published version.

2. Material and methods

In the following, the most significant parts of our methodology are summarized. A comprehensive description of the reconstruction and post-processing algorithms can be found in Pennazio *et al* (2022). The simulated setup and the procedure to estimate the stopping power are described in detail in Ferrero *et al* (2022b).

2.1. Monte-Carlo simulation and reconstruction

The geometry and scintillator detectors were modelled using FLUKA (Ferrari *et al* 2005, Böhlen *et al* 2014). A total of 110 monolithic cylindrical Cerium-doped Lanthanum bromide ($LaBr_3$:Ce) crystals were placed in the asymmetric pattern shown in figure 1, which is repeated five times along the y-axis. The event post-processing accounted for a time and energy resolution of 250 ps FWHM and $\sigma_E/E = 4\%$. The simulated irradiation covered the energy range $[63\,\text{MeV}, 219\,\text{MeV}]$ in steps of about 10 MeV. For each beam energy, we ran 50 realizations (10^7 protons per run). This study therefore significantly extends our previous work towards lower energies, where the lower photon emission makes its reconstruction more challenging.

To reconstruct the spatiotemporal distribution from the PGT spectra, we apply the iterative algorithm Maximum-Likelihood Expectation-Maximization (ML-EM) combined with a system response model calculated through Monte-Carlo simulations. The SER-PGT output is a depth-time histogram (2D): The intensity of a specific pixel corresponds to the estimated number of PG emitted during a certain time interval around t from a certain spatial bin centered at depth z. A threshold T relative to the maximum of the reconstructed distribution is applied. For each time interval, the center of gravity is calculated to get position and time pairs $[z, t]$. SER-PGT could be expanded to include the transversal dimensions, but this would increase the number of unknowns while the amount of available data would not change, thus compromising the accuracy of the estimates. At the current stage of our research, the current approach, which restricts the PG to the beam axis, is sufficient to extract the particle range and motion.

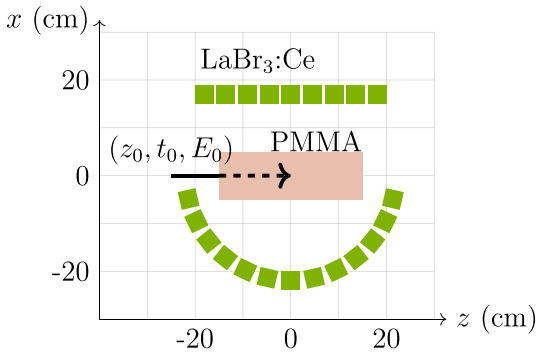

Figure 1. Lateral view of the simulated setup: PMMA phantom (red), asymmetric detector pattern (green) and proton beams emitted in the direction of the positive z-axis from position $(z_0, 0, 0)$ at time t_0 with kinetic energy E_0.

2.2. Stopping power estimation

We use an analytical approximation of the particle kinetic energy along its depth for homogeneous materials, following Bortfeld (1997),

$$E(\hat{z}) = \sqrt[p]{\frac{R_0 - \hat{z}}{\alpha}}, \tag{1}$$

where E is the particle energy at depth $\hat{z}$, and α and p are free parameters linked to the range R_0 and the initial energy E_0 through $R_0 = \alpha E_0^p$. The derivative of equation (1) corresponds to the stopping power. To reduce the number of free parameters in the motion model, R_0 is calculated beforehand as the z of the last $[z, t]$ pair.

In Ferrero *et al* (2022b), we developed an analytical solution to equation (1) to obtain the motion as $t(z)$. Fitting this function to the $[t, z]$ points extracted from the SER-PGT output yields the α and p to be inserted in the derivative of equation (1) for the calculation of the stopping power. The function domain of $t(z)$ is inherently limited to $[-\infty, z_0 + R_0]$ with z_0 the position at which the beam enters the material. During the fitting process, positions beyond the range $R_0 = \alpha E_0^p$ are likely to be evaluated. The return values chosen for these cases can penalize or favor non-physical solutions of the fitting problem, and therefore produce incorrect estimations of the stopping power.

Here, we achieve an unbounded and physically sensible function domain by solving the relativistic motion equation to obtain $z(t)$. This also allows us to account for the uncertainty along z, visible in figure 2 when fitting the model to the reconstructed emission distribution. Usually, the velocity is integrated over time to calculate the position as a function of time. We assume the particles only travel along the beam axis, simplifying the problem to integrating the speed. Unfortunately the speed v needs to be calculated based on equation (1) which only yields the speed as a function of the depth. Therefore, $z(t)$ would need to be known to calculate $v(t)$. Due to this contradiction we decided to use the numerical approximation

$$z(t) = \int_{t_0}^{t} v(t)\,\mathrm{d}t + z_0 \approx \Delta t \sum_{j=1}^{J} v\left(z\left(t_{j-1}\right)\right) + (t - t_J)\, v(z(t_J)) + z_0; \quad v(z_0) = v(E_0), \tag{2}$$

with v the speed of the particle, uniquely defined either by its relativistic kinetic energy ($v(E)$), time ($v(t)$) or position ($v(z)$); Δt is the step size, with $J = \left\lfloor \frac{t - t_0}{\Delta t} \right\rfloor$ evenly-spaced samples between t_0 and t. Once position $z(t_{j-1})$ is calculated, the speed v at that depth is known based on equation (1). The next position $z(t_j)$ is approximated as $z(t_j) = z(t_{j-1}) + \Delta t\, v(z(t_{j-1}))$, assuming a constant speed within the time interval $[t_{j-1}, t_j)$. This process is repeated until the time t is reached. The accuracy of this approximation is compared to the analytical implementation of $t(z)$ for 0 MeV–250 MeV proton beams in water (section 3.3). A time step of $\Delta t = 2.5$ ps was found to be a good compromise between execution speed and accuracy.

We will refer to the implementation of Ferrero *et al* (2022b) as the TimeFit procedure and the new implementation using equation (2) as the PositionFit procedure.

2.3. Figures of merit

We have analyzed the results using three figures of merit (FoMs): the mean relative error (MRE) of the stopping power profile, the error of the stopping power ratio (SPR), ΔSPR, and the difference between true and estimated range, ΔR. The NIST PSTAR database (Berger *et al* 2005) was used to provide the reference values. The range error ΔR was calculated as in Ferrero *et al* (2022b). There we also introduced the MRE, but here we modified the implementation to evaluate the stopping power profile up to $\max(R_{\mathrm{NIST}}, R_E)$. This

ensures equal penalization of overestimation and underestimation of the reconstructed range R_E. The stopping power ratio (SPR) error was calculated with respect to water at 100 MeV as suggested in Peters *et al* (2023). After calculating the FoMs for all realizations, we computed their mean, standard deviation, and minimum and maximum value for each considered energy.

2.4. Automated hyperparameter optimization

The values in the post-processed 2D histogram depend on the number of ML-EM iterations, k, and the threshold T. To determine the best suited values of k and T, we have studied different optimization criteria based on the three FoMs. These hyperparameters are chosen independently for each primary beam energy, since effects like differing number and distribution of emitted and detected particles affect the ML-EM reconstruction features. In Ferrero *et al* (2022b), the hyperparameters were chosen manually. Here, we test two approaches to automatically determine parameters that yield the best results across multiple datasets: risk-sensitive and scenario-based optimization. Note that in our implementation the optimal values of the hyperparameters can only be identified if the ground truth is available. In a real application, these parameters should be pre-set based on calibration or simulation data.

In risk-sensitive optimization, the mean μ_{FoM} and standard deviation σ_{FoM} of a specific FoM over a set of samples $\{\Delta_n\}_{n=1,\dots,N}$ as a function of k and T is minimized:

$$(\hat{k},\hat{T})_{\text{risk-sensitive}} = \underset{(k,T)}{\operatorname{argmin}} \left(|\mu_{\mathrm{FoM}}| + w_\sigma \sigma_{\mathrm{FoM}}\right), \tag{3}$$

with risk-aversion parameter $w_\sigma \geqslant 0 \in \mathbb{R}$ (Boyd and Vandenberghe 2004). We used $w_\sigma = 1$.

The scenario-based approach minimizes the error in the worst-case scenario, i.e. the highest loss encountered in all realizations (Campi and Garatti 2018). Since all FoMs represent errors and should therefore be minimized, we arrive at

$$(\hat{k},\hat{T})_{\text{scenario-based}} = \underset{(k,T)}{\operatorname{argmin}} \max_{\{\Delta_n\}_{n=1,\dots,N}} |\mathrm{FoM}(\Delta_n)|, \tag{4}$$

i.e. minimizing the loss of the worst performance across all realizations.

We evaluated all combinations of 1–100 iterations and relative thresholds $T \in [0, 0.8]$ in steps of $\Delta k = 1$ and $\Delta T = 0.025$, respectively. Solving the problems given in equations (3) and (4) numerically boils down to calculating the respective objective function for all 3300 parameter combinations.

3. Results

3.1. Reconstructed distributions across the therapeutical energy range

Figure 2 shows exemplary SER-PGT distributions of four selected energies. Such distributions are the basis for estimating the particle range and average motion, and thereby the stopping power. For short ranges (figures 2(a) and (b)), the reconstructed distributions are very small, so the average particle motion is not clearly visible. For 160 MeV the motion becomes recognizable, and for 219 MeV the curvature of the distribution clearly shows the slowing down of the particles towards the end of the particle range.

Figures 2(c) and (d) show signs of the Gibbs phenomenon, in particular at the entrance of the phantom (high-intensity region at low t and z values). Such artifacts are known to affect ML-EM-based image reconstruction when there is a close match between the calculated and true system response model (Tong *et al* 2011). Our system response model for SER-PGT was calculated using Monte-Carlo simulations and uses the same time and energy resolution as the PGT-data from our proton beam simulations. The reconstructed distribution at 63 MeV is almost completely contained in areas affected by the Gibbs artifacts.

3.2. Range estimation error

Figure 3 shows the average, maximum, and minimum range error, as well as the corresponding standard deviations for all beam energies after optimization. Additionally, we calculated the range estimation error for the manually selected hyperparameters from Ferrero *et al* (2022b) using all realizations. For all but the lowest beam energy (63 MeV) the mean range error lies within ± 2 mm. The maximum absolute range error is within ± 10 mm for both optimization approaches. Also, the standard deviations consistently lie between 2 mm–3 mm for all energies except 63 MeV. Both formulations show little to no energy-dependence for all other energies and match the previously reported standard deviation of 3 mm while reducing the maximum observed deviation by up to 5 mm.

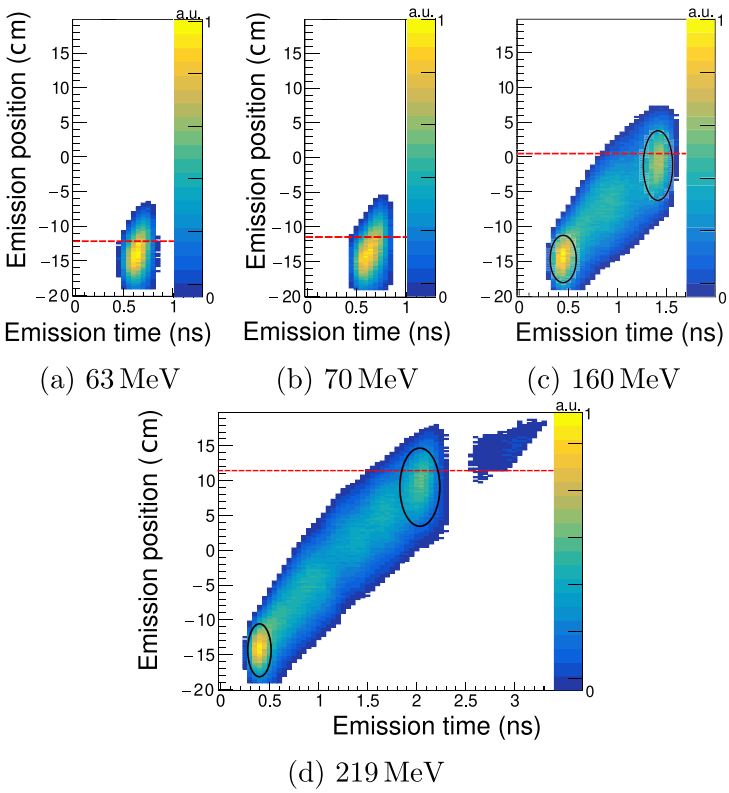

Figure 2. Exemplary reconstructed spatiotemporal emission distributions after 30 iterations and a threshold of 10% for selected energies. Emission positions (ordinate) are given along the beam direction. The expected particle range is marked with a red dashed line and the range of the abscissa is adapted to each case. Examples of the Gibbs phenomenon are encircled with black lines. For visualization purposes only, the parameters were selected manually.

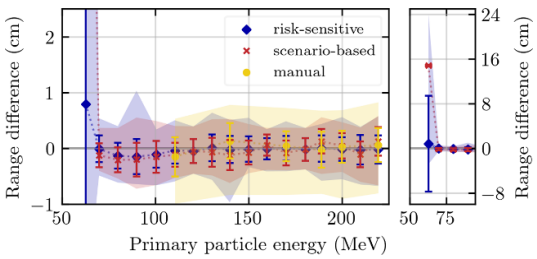

Figure 3. Error of the range estimate ΔR using hyperparameters optimized with risk-sensitive (⧫) and scenario-based optimization (×), and manual selection from Ferrero *et al* (2022b) (●). Markers represent the mean, whiskers the standard deviation, and the colored area the minimum and maximum of the range error. Lines between data points are for visualization purposes only. The insert on the right shows errors on a larger scale.

3.3. New implementation of the motion model

Since both implementations of the motion model are based on equation (1), evaluating $z(t(z))$ should recover the original z. Small deviations are to be expected from the discretization of the speed when calculating $z(t)$, as shown in figure 4. Figure 4(b) shows that when using 2.5 ps time steps, the deviation between the analytical and numerical implementation does not exceed 0.1 mm even for 250 MeV in water.

3.4. Stopping power estimates

Figure 5 shows the FoMs related to the stopping power estimation. We also calculated the FoMs for the manually selected hyperparameters from Ferrero *et al* (2022b) for the TimeFit procedure. Differences between the two procedures for hyperparameter optimizations are marginal for 100 MeV and above, in some cases even returning the same hyperparameters. For lower energies, we observe errors of 30% and more. The mean and standard deviation resulting from the automated optimization are similar to the results of the manual selection, but the maximum errors of the automatic optimization are 5%–10% lower in almost all cases.

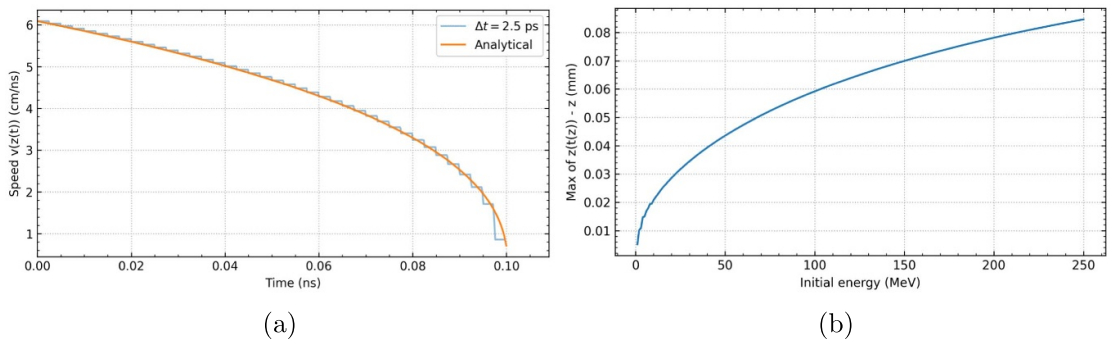

Figure 4. (a) Analytical and discretized speed profiles from equation (2) for 20 MeV protons in water. (b) Maximum error when inverting $t(z)$ with the $z(t)$ implementation for protons in water as a function of initial particle energy.

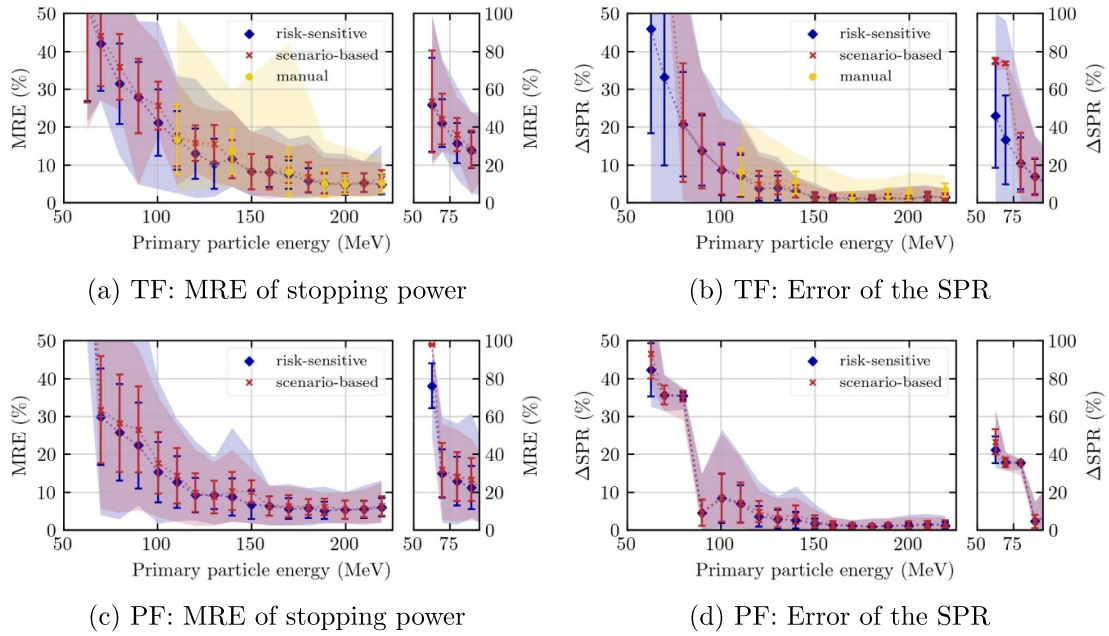

Figure 5. MRE and ΔSPR of the Timefit (TF, top row) and PositionFit (PF, bottom row) procedures using hyperparameters optimized for each FoM. The visualization of the errors follows the logic described in the caption of figure 3.

For beam energies larger than 100 MeV, the SPR obtained through the two hyperparameter optimizations and the two implementations of the motion model shows no significant differences. Above 160 MeV, the mean error of the SPR approaches 1% for all techniques, and the maximum deviation among all realizations does not exceed 5%.

The MRE shows a similar dependency on the beam energy. For 160 MeV and above, the TimeFit procedure approaches a mean MRE of $6 \pm 2\%$ with maximum errors ranging from 10% to 20%. The PositionFit procedure with the new motion model shows very stable performance from 160 MeV to 220 MeV, with a mean MRE of $5 \pm 2\%$ and maximum errors from 10% to 12%. For energies below 160 MeV, PositionFit outperforms TimeFit by a few percent, and both fail to give precise and accurate stopping power estimates for beam energies below 100 MeV. The execution of PositionFit was up to eight times slower than the TimeFit, but its 8.3 ± 0.3 ms per distribution is still quick enough to enable fast evaluation of the acquired data.

4. Discussion

For all FoMs, the new automated hyperparameter optimization reduces the maximum errors compared to our former manual selection, reported in Ferrero *et al* (2022b). In that work, only the mean of the MRE was used for manual selection, while the ΔSPR had not been introduced yet. Currently, the hyperparameters are optimized for a specific case, e.g. a combination of the number of particles, initial particle energy as well as

target composition and position. It remains to be studied how sensitive the estimation performance is to differences between the scenarios considered during the evaluation procedure and the actual application. This transfer is crucial since the clinical application requires the parameters to be fixed beforehand. Nevertheless, automated parameter selection eliminates the need for manual intervention during the evaluation stages. Within this study, the automation serves to understand the theoretical performance limit of SER-PGT and the impact of changes to the estimation procedure. Thanks to this hyperparameter optimization, we can evaluate future changes to the estimation procedures in a reproducible, objective and time-efficient manner.

Earlier works have shown range estimates based on PGT measurements for few proton beam energies or full treatment plans, reporting e.g. standard deviations of 2 mm (Jacquet *et al* 2021) and 3 mm–5 mm (Pennazio *et al* 2022, Ferrero *et al* 2022b) for 10^7 protons, and a RMSE of 4 mm for 10^8 protons (Schellhammer *et al* 2022). Here, we have systematically studied the beam-energy dependence of our range estimates across the common therapeutic energy range. Safety margins applied in treatment planning usually include a component proportional to the particle range (Paganetti 2012). Our results showing a range estimate with (mostly) energy-independent precision and accuracy, as observed in figure 3, encourage further verification in heterogeneous targets.

By introducing the relative error of the SPR, we can now compare our stopping power estimations directly to modalities used in treatment planning. For beam energies above 160 MeV, we observe estimation errors close to the 1%–4% uncertainty of the NIST PSTAR stopping power reported by Berger *et al* (1993). Within that energy range, the observed performance was independent of the applied optimization strategy. While the risk-aware optimization allows a user-defined trade-off between accuracy and precision, the scenario-based approach only depends on the number of datasets used.

Hyperparameter automation has allowed us to efficiently expand the number of evaluated kinetic particle energies from 6 to 17, covering almost the full operational range for protons of 63 MeV–229 MeV at the CNAO treatment center (Mirandola *et al* 2015). The results indicate limitations of our current implementation for both range and stopping power estimation for beam energies below 70 MeV and 120 MeV, respectively. The poor performance at low beam energies was not solved by the new implementation of the motion model. It did however stabilize the estimation accuracy and precision to consistently satisfactory levels for beam energies from 150 MeV to 200 MeV, thereby expanding the energy range to which PGT-SPE may be applied. The large errors for energies below 120 MeV might be reduced by considering the multiple beams with different energies passing through the same transversal spot simultaneously.

The simulation has shown good agreement with experimental data in Ferrero *et al* (2023). The thin silicon detectors tag single particles with a time resolution of 30 ps (Vignati *et al* 2023) and the PG-detectors show a time resolution of 124 ps (Ferrero *et al* 2022a). Therefore, the resulting coincidence time resolution is only slightly larger than the 106 ps applied in this work. Further limitations of the simulation are discussed in Ferrero *et al* (2022b). The parameter optimization, incremental performance improvements, and extension of the evaluated energies are important stepping stones towards demonstrating the technique with heterogeneous phantoms.

5. Conclusion

Hyperparameters of PGT-SPE were optimized automatically, replacing the time-consuming and subjective manual choice of hyperparameters used in Ferrero *et al* (2022b). The automation lead to a reduction of the maximum observed errors. We also implemented an alternative stopping power estimation procedure based on formulating the mean particle position as a function of time, reducing the estimation errors by a few percent. For both implementations, the stopping power estimation for beam energies of 120 MeV and below remains unsatisfactory, with errors exceeding 12%. For 160 MeV and above, the SPR estimation errors match the accuracy of the reference stopping power of 1%–5%. Range estimation performance was largely independent of the primary particle energy and showed a standard deviation of 3 mm.

Data availability statement

All data that support the findings of this study are included within the article (and any supplementary information files).

Acknowledgments

This work was supported in part by the INFN Group 5 Young Investigators Grant MERLINO No. 23246/21, the German Research Foundation (DFG) by Grants No. 516587313 (PROSIT) and No. 383681334 (COMMA), the Cluster of Excellence EXC 2167 (Project No. 390884018), and a mobility fellowship within the IFI programme of the German Academic Exchange Service (DAAD).

Conflict of interest

All authors declare that they have no known conflicts of interest in terms of competing financial interests or personal relationships that could have an influence or are relevant to the work reported in this paper. This study did not involve human participants or animal experimentation.

ORCID iDs

Julius Werner https://orcid.org/0000-0002-2389-0371
Francesco Pennazio https://orcid.org/0000-0001-8323-0132
Niklas Schmid https://orcid.org/0000-0002-8068-6967
Elisa Fiorina https://orcid.org/0000-0002-8172-4283
Davide Bersani https://orcid.org/0009-0007-3773-4699
Piergiorgio Cerello https://orcid.org/0000-0002-2443-5178
Jona Kasprzak https://orcid.org/0000-0002-2075-3232
Nicola Mosco https://orcid.org/0000-0001-6091-2130
Sahar Ranjbar https://orcid.org/0009-0000-9998-4094
Roberto Sacchi https://orcid.org/0000-0001-7794-0170
Veronica Ferrero https://orcid.org/0000-0003-3900-6680
Magdalena Rafecas https://orcid.org/0000-0001-5691-7756

References

Berger M, Coursey J, Zucker M and Chang J 2005 *ESTAR, PSTAR, and ASTAR: Computer Programs for Calculating Stopping-Power and Range Tables for Electrons, Protons, and Helium Ions (version 1.2.3)* (National Institute of Standards and Technology) (https://doi.org/10.18434/T4NC7P)

Berger M, Inokuti M, Andersen H and Bichsel H 1993 ICRU report 49: stopping powers and ranges for protons and alpha particles *J. Int. Comm. Radiat. Units Meas.* **os-25** 48–60

Böhlen T, Cerutti F, Chin M, Fassò A, Ferrari A, Ortega P G, Mairani A, Sala P R, Smirnov G and Vlachoudis V 2014 The FLUKA code: developments and challenges for high energy and medical applications *Nucl. Data Sheets* **120** 211–4

Bortfeld T 1997 An analytical approximation of the Bragg curve for therapeutic proton beams *Med. Phys.* **24** 2024–33

Boyd S and Vandenberghe L 2004 *Convex Optimization* (Cambridge University Press) ch 4, pp 154–5

Campi M C and Garatti S 2018 *Introduction to the Scenario Approach* (SIAM) ch 1, pp 1–20

Ferrari A, Sala P R, Fassò A and Ranft J 2005 FLUKA : A multi-particle transport code CERN-2005-10 (https://doi.org/10.5170/CERN-2005-010)

Ferrero V *et al* 2023 Proton therapy treatment verification: a spatio-temporal emission reconstruction with experimental data *2023 IEEE Nuclear Science Symp., Medical Imaging Conf. and Int. Symp. on Room-Temperature Semiconductor Detectors (NSS MIC RTSD)* pp 1–2

Ferrero V, Werner J, Aglietta M, Cerello P, Fiorina E, Gorgi A, Vignati A, Rafecas M and Pennazio F 2022a The MERLINO project: characterization of $LaBr_3$:Ce detectors for stopping power monitoring in proton therapy *J. Instrum.* **17** C11013

Ferrero V, Werner J, Cerello P, Fiorina E, Vignati A, Pennazio F and Rafecas M 2022b Estimating the stopping power distribution during proton therapy: a proof of concept *Front. Phys.* **10** 971767

Golnik C *et al* 2014 Range assessment in particle therapy based on prompt γ-ray timing measurements *Phys. Med. Biol.* **59** 5399

Jacquet M *et al* 2021 A time-of-flight-based reconstruction for real-time prompt-gamma imaging in proton therapy *Phys. Med. Biol.* **66** 135003

Mirandola A *et al* 2015 Dosimetric commissioning and quality assurance of scanned ion beams at the Italian National Center for Oncological Hadrontherapy *Med. Phys.* **42** 5287–300

Paganetti H 2012 Range uncertainties in proton therapy and the role of Monte Carlo simulations *Phys. Med. Biol.* **57** R99

Pennazio F *et al* 2022 Proton therapy monitoring: spatiotemporal emission reconstruction with prompt gamma timing and implementation with PET detectors *Phys. Med. Biol.* **67** 065005

Peters N *et al* 2023 Consensus guide on CT-based prediction of stopping-power ratio using a Hounsfield look-up table for proton therapy *Radiother. Oncol.* **184** 109675

Schellhammer S M, Wiedkamp J, Löck S and Kögler T 2022 Multivariate statistical modelling to improve particle treatment verification: implications for prompt gamma-ray timing *Front. Phys.* **10** 932950

Tong S, Alessio A M, Thielemans K, Stearns C, Ross S and Kinahan P E 2011 Properties and mitigation of edge artifacts in PSF-based PET reconstruction *IEEE Trans. Nucl. Sci.* **58** 2264–75

Vignati A *et al* 2023 Calibration method and performance of a time-of-flight detector to measure absolute beam energy in proton therapy *Med. Phys.* **50** 5817–27

Werner T *et al* 2019 Processing of prompt gamma-ray timing data for proton range measurements at a clinical beam delivery *Phys. Med. Biol.* **64** 105023